



Mechanistic understanding of cellulose β -1,4-glycosidic cleavage via photocatalysis



Heng Zhao ^{a,b,1}, Chao-Fan Li ^{b,1}, Xinti Yu ^a, Na Zhong ^a, Zhi-Yi Hu ^{b,c,*}, Yu Li ^b, Stephen Larter ^d, Md Golam Kibria ^{a, **}, Jinguang Hu ^{a, **}

^a Department of Chemical and Petroleum Engineering, University of Calgary, 2500 University Drive, NW, Calgary, Alberta T2N 1N4, Canada

^b State Key Laboratory of Advanced Technology for Materials Synthesis and Processing, Wuhan University of Technology, 122 Luoshi Road, 430070 Wuhan, Hubei, China

^c Nanostructure Research Centre (NRC), Wuhan University of Technology, 122 Luoshi Road, 430070 Wuhan, Hubei, China

^d Department of Geosciences, University of Calgary, 2500 University Drive, NW, Calgary, Alberta T2N 1N4, Canada

ARTICLE INFO

Keywords:

Biomass photorefinery
Cellulose photoreforming mechanism
Celloolose photoreforming
Artificial photocatalyst
Z-scheme heterojunction

ABSTRACT

Photoreforming of lignocellulosic biomass is an emerging and sustainable strategy for coproduction of high-value chemicals and fuels. Challenges remain to selectively convert biomass macromolecular via sunlight-driven photocatalysis due to limited mass diffusion, insufficient charge separation and lack of mechanistic understanding. Herein, inspired by natural photosynthesis, we demonstrate a hierarchically threedimensionally ordered macroporous (3DOM) TiO_2 -Au-CdS Z-scheme heterojunction photocatalyst to improve mass diffusion, charge separation and light absorption efficiency. We show the photocatalytic cleavage pathway of cellulose β -1,4-glycosidic linkage (the most abundant linkage within biomass) over 3DOM TiO_2 -Au-CdS heterojunction by using celloolose as a model component. Similar to the oxidative enzymes in nature, the all-solid-state Z-scheme photocatalyst demonstrates oxygen insertion at C1 position followed by the elimination reaction, which oxidatively cleaves the β -1,4-glycosidic bond and results in gluconic acid and glucose generation. In presence of oxygen, glucose is further oxidized into gluconic acid which is subsequently oxidized or decarboxylated into glucaric acid or arabinose. The present study may serve as a framework to rationally design photocatalyst to reveal mechanistic understanding of biomass photoreforming towards high-value fuels and chemical feedstocks.

1. Introduction

Efficient lignocellulosic biomass valorization into high-value chemicals and fuels provides a promising alternative to accelerate transition from traditional fossil-fuel to renewable energy sources [1,2]. Biomass photoreforming, a novel low carbon biorefinery strategy to convert biomass to valuable chemicals along with gas fuels (such as hydrogen) coproduction via solar energy, has attracted great attention recently [3–7]. Although photoreforming of soluble organic feedstocks derived from biomass (e.g. glucose [8], alcohol [9], HMF [10] etc.) have been demonstrated, direct photoreforming of insoluble lignocellulosic materials remains challenging [11]. We and others have recently demonstrated the feasibility of sunlight driven photoreforming of raw/processed lignocellulosic biomass to H_2 using nanoengineered

heterogeneous photocatalysts [12–15]. However, the lack of clear mechanistic understanding of lignocellulose degradation pathways as well as the inefficient mass diffusion and light capture ability of photocatalyst impedes practical application of biomass valorization via the photorefinery concept.

Cellulose, a linear polymer of D-glucose connected via β -1,4 glycosidic bonds, is the most abundant biomass components in nature [16, 17]. Although many works have already been conducted by using glucose as the model component to uncover the mechanism of cellulose photoreforming [14,18–20], this approach can't reveal the photocatalytic reaction pathway for the cellulose polymer cleavage. Celloolose, a disaccharide with the glucose residues rotated 180° relative to each other and joined via β -1,4-glycosidic bonds along the main axis, is the basic repetitive units of cellulose [21]. Up to now, celloolose

* Corresponding author at: Nanostructure Research Centre (NRC), Wuhan University of Technology, 122 Luoshi Road, 430070 Wuhan, Hubei, China.

** Corresponding authors.

E-mail addresses: zhiyi.hu@whut.edu.cn (Z.-Y. Hu), md.kibria@ucalgary.ca (M.G. Kibria), jinguang.hu@ucalgary.ca (J. Hu).

¹ These two authors contribute equally to this work.

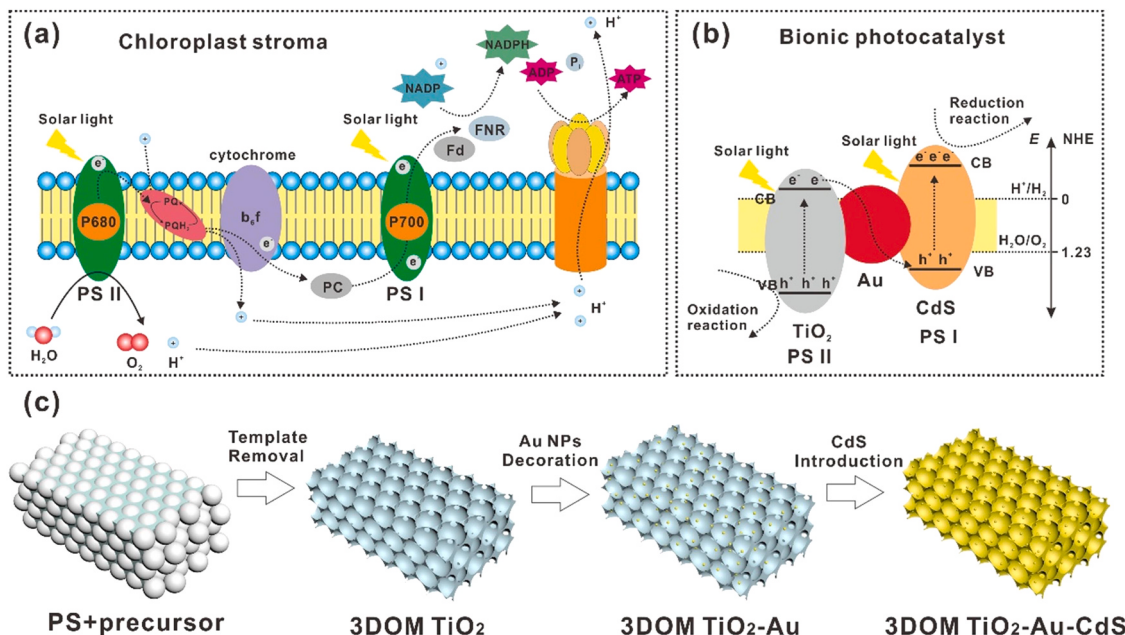


Fig. 1. Schematic illustrations of (a) photosynthesis process in natural chloroplast stroma, (b) charge transfer pathway in and (c) preparation process of 3DOM TiO₂-Au-CdS.

thermcatalytic and biocatalytic conversion pathways have been well studied [22–24]. For example, efficient hydrolysis of β -1,4-glycosidic bonds of cellobiose was realized on PdCl₂-CuCl by thermocatalysis [25]. However, to the best of our knowledge, there has been limited studies on cellobiose photocatalytic conversion mechanism.

Along with understanding biomass photo-degradation pathway, it is also crucial to design and fabricate suitable photocatalysts with desired properties (e.g. easy mass diffusion, light harvesting, enhanced charge separation etc.) for biomass photoreforming [15,26,27]. In this context, hierarchical 3DOM structures are appealing as they offer enhanced light harvesting by multiple scattering of incident light and slow photon effect [28,29]. Besides, as a typical Murray material, the inter-connected porosity of 3DOM structure endows the photocatalyst with excellent mass diffusion property, which increases the accessibility of biomass macromolecular [30,31]. Efficient charge separation is another crucial factor to improve photocatalytic quantum efficiency [32,33]. Inspired by natural chloroplast stroma of photosystem, all-solid-state Z-scheme structure stands out in spatial charge separation by utilizing the advantages of heterojunction structure [34–37]. Although Z-scheme photocatalysts have been used for various solar-driven applications such as hydrogen production [38], CO₂ reduction [39], and wastewater treatment [40], their potential application for biomass photoreforming has yet to be explored.

Herein, we report an all-solid-state Z-scheme 3DOM TiO₂-Au-CdS to explore the mechanism of cellobiose photocatalytic conversion. We demonstrate that the cleavage of β -1,4-glycosidic bond was initiated by oxygen insertion at C1 position, leading to the generation of glucose and gluconic acid. The electron spin resonance (ESR) and scavenger trapping experiments demonstrated that the photogenerated-O₂[·] and OH played a synergistic effect for cellobiose photoreforming. Along with cellobiose conversion, considerable amount of gas products (H₂, CH₄, CO etc.) were also produced. The present work not only provides an in-depth mechanistic understanding of β -1,4 bond breakage but also sheds new light on rational photocatalyst design to simultaneously produce valuable chemicals and gas fuels via biomass photoreforming.

2. Experimental

2.1. Preparation of 3DOM TiO₂-Au-CdS

Photocatalyst preparation is according to our previous reports [29, 36,41]. Briefly, polystyrene (PS) spheres were synthesized through surfactant-free emulsion polymerization and assembled into opal structure as colloid template. The precursor of TiO₂ filled the interspace of PS spheres and the 3DOM TiO₂ was obtained after sol-gel process and calcination in air to remove PS template. Au NPs were decorated on the surface of 3DOM TiO₂ by sodium citrate reduction method. Finally, CdS was introduced by chemical bath deposition of cadmium nitrate and sodium sulfide. Detailed process of photocatalyst preparation could be found in [Supporting information](#).

2.2. Characterization

Scanning electron microscope (SEM) was performed on Hitachi S-4800 while the aberration corrected transmission electron microscope (TEM) was conducted on Thermo Fisher Titan Themis. Power X-ray diffraction (XRD, D8 ADVANCE) was used to investigate the crystalline structure of photocatalysts. Micromeritics surface area and porosity analyzer were used to quantify the specific surface areas pore-size distributions respectively. The UV-Vis absorption spectra of different photocatalysts were collected on SHIMADZU UV-Vis spectrophotometer while the steady photoluminescence (PL) spectra were collected at excitation wavelength of 300 nm on a fluorescence spectrophotometer (PerkinElmer, LS-55). PerkinElmer Frontier was used to record the Fourier-transform infrared spectroscopy (FTIR) spectra in the range of 4000–500 cm⁻¹. X-ray photoelectron spectroscopy (XPS) was performed on Thermo Fisher spectrometer and C 1 s at 284.8 eV was used as calibration. The presence of oxygen-contained radicals during the photocatalytic reaction was revealed by electron spin-resonance (ESR) spectroscopy. Bruker Advance III 400 spectrometer was used to record the ¹³C nuclear magnetic resonance (NMR) signals.

2.3. Photocatalytic measurement

Typically, 10 mg photocatalyst was dispersed in the 25 mL 2 g/L

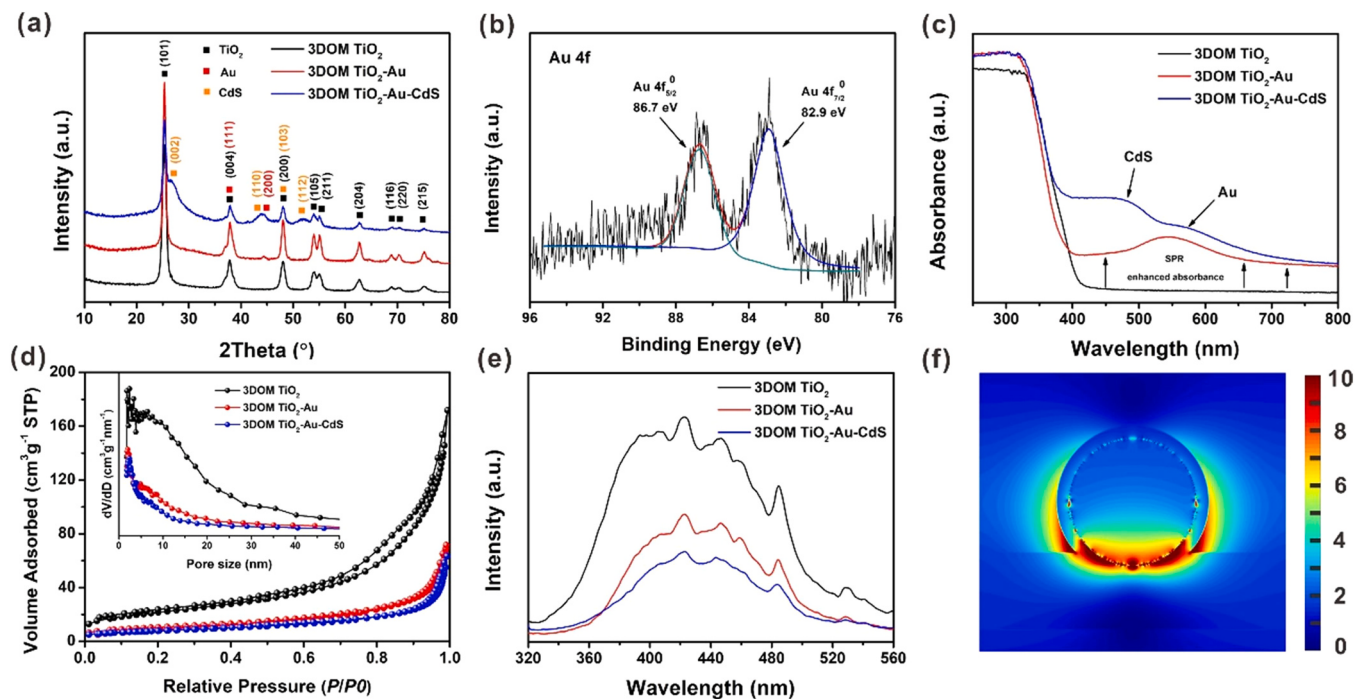


Fig. 2. (a) XRD patterns, (b) XPS spectrum of Au 4 f in 3DOM TiO₂-Au-CdS, (c) UV-vis absorption spectra, (d) N₂ absorption-desorption isotherms (inset is the corresponding mesopore distribution), (e) PL spectra of 3DOM TiO₂, 3DOM TiO₂-Au and 3DOM TiO₂-Au-CdS and (f) simulated distribution of electromagnetic field intensity at 550 nm of 3DOM TiO₂-Au-CdS.

cellobiose solution and the suspension was vacuumed with sonication for 0.5 h before light irradiation by a 300 W PLS-SXE-300 Xenon lamp (320–780 nm, 2.1 W/cm², Beijing Perfectlight). The headspace was changed by bubbling with argon, air or oxygen for 0.5 h before reaction. The gas products were periodically analyzed and quantified by a gas chromatography (GC, Clarus 590, PerkinElmer) with a 5 A Molecular Sieve and a Carboxen 1000 packed column. The produced H₂ and CO were quantified by a thermal conductivity detector (TCD) while the produced CH₄, C₂H₄ and C₂H₆ were analyzed by a flame ionization detector (FID). 0.5 mL of reaction solution was periodically sampled and centrifuged to remove photocatalyst for further test. The cellobiose concentration and liquid products were monitored by high-performance liquid chromatography (HPLC, 1200 Agilent system), which was equipped with a refractive index detector (RID). The corresponding column was Aminex HPX-87H (300 × 7.8 mm, Bio-Rad) and the mobile phase was 5 mM sulfuric acid at a flow rate of 0.6 mL/min.

2.4. Finite-difference time-domain (FDTD) simulation

FDTD method was adopted by using the commercial FDTD-Lumerical™ simulation package to simulate the electromagnetic field distribution nearby Au NPs. 550 nm was selected as the excitation wavelengths based on the light absorbance spectra, and the mesh size was set as 0.5 nm for this calculation. The geometrical parameters of the ternary photocatalyst were modeled based on the experimental results from SEM, TEM and XPS. The dielectric constants of CdS and TiO₂ were set as 2.5 and 2.6 respectively and the calculations were performed in air condition.

3. Results and discussion

3.1. Catalyst design

Natural photosynthesis provides a good concept to design photocatalysts with excellent charge separation efficiency. Two light responsible components (PS I and PS II) and electron transfer media

(cytochrome) construct Z-scheme electron transfer pathway (Fig. 1a). Inspired by the natural photocatalysts, here we developed all-solid-state Z-scheme by combining two semiconductors in which TiO₂ acted as PS II while CdS as PS I and Au NPs as the electron transfer media (Fig. 1b) [29, 34–36]. Besides, the presence of Au NPs could also improve light harvesting and extend light absorption region because of the surface plasmon resonance (SPR) effect [35, 41, 42]. Combining the advantages of hierarchical structure in light harvesting and mass diffusion, 3DOM TiO₂-Au-CdS is designed and fabricated as schematically illustrated in Fig. 1c. The prepared PS spheres were assembled into opal structure with uniform diameter of 340 nm (Fig. S1a). The uniformity of PS colloid template in opal structure directly leads to the completeness of the inverse opal 3DOM structure for photocatalyst (Fig. S1). The obtained 3DOM TiO₂-Au-CdS shows inter-connected and ordered macroporous structure in the long range, which would facilitate mass diffusion and light harvesting (Fig. S1b).

3.2. Catalyst characterization

The components and crystallographic phases as well as crystallinity of each photocatalyst during 3DOM TiO₂-Au-CdS synthesis were investigated by XRD (Fig. 2a). 3DOM TiO₂ showed characteristic diffraction peaks of pure anatase crystalline phase with high crystallinity. Typical diffraction peaks at around 43.4°, 63.0° and 75.6° (2θ) were identified for Au (200), (220) and (311) after decorating Au NPs on the surface of 3DOM TiO₂ (Fig. S2). Typical peaks of wurtzite structured hexagonal CdS were clearly observed in the final Z-scheme 3DOM TiO₂-Au-CdS. The chemical state of Au NPs is metallic as confirmed by the XPS results (Fig. 2b). Apart from the lattice oxygen, the high resolution XPS of O1s revealed the presence of oxygen vacancy (531.6 eV) in the as-fabricated 3DOM TiO₂-Au-CdS (Fig. S3). Besides, oxidized sulfur species of SO₃²⁻ or SO₄²⁻ (168.7 eV) were partially present along with S²⁻ (161.4 eV) in CdS. The presence of Au NPs endows 3DOM TiO₂ with enhanced visible light absorption efficiency due to the SPR effect (Fig. 2c). For the ternary 3DOM TiO₂-Au-CdS, the typical light absorption edges for TiO₂ and CdS as well as the SPR absorption of Au NPs could be clearly identified

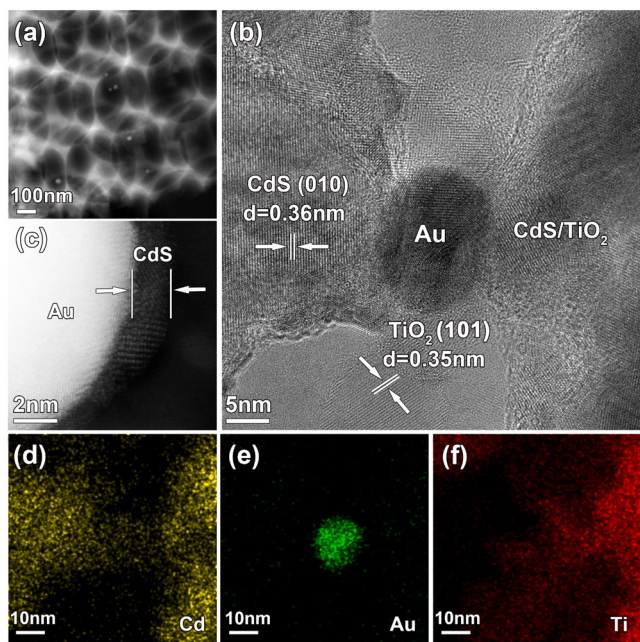


Fig. 3. (a) HAADF-STEM image, (b) HR-TEM image, (c) HR-HAADF-STEM image, (d-f) corresponding EDS elemental maps of the area in (b): Cd (yellow), Au (green) and Ti (red), respectively.

(Fig. 2c). The typical Tauc plots calculated from UV-vis spectra were shown in Fig. S4. The hierarchical 3DOM structure exhibits relatively large specific surface area ($76.6 \text{ m}^2/\text{g}$ for 3DOM TiO_2). Even though the introduction of Au NPs and CdS could partially collapse the hierarchical porous structure, the ternary 3DOM TiO_2 -Au-CdS still hold relatively high specific surface area $28.1 \text{ m}^2/\text{g}$ (Fig. 2d). The advantage of Z-scheme heterojunction is to improve photogenerated charge separation, which was evidenced by the significantly reduced PL intensity (Fig. 2e) [34,43]. To further confirm the charge separation ability of Au NPs in this ternary photocatalyst, the electromagnetic field distribution around a single gold nanoparticle was exhibited by finite-difference time-domain (FDTD) method using Maxwell's equations [44]. Obviously, the electromagnetic field at the interfaces of TiO_2 /Au and Au/CdS was much enhanced, indicating that the presence of Au NPs indeed act as the electron transfer media to improve the spatial separation of photo-generated electrons and holes (Fig. 2f and S5). Thus, the well-designed 3DOM TiO_2 -Au-CdS Z-scheme heterojunction with the combination of improved mass diffusion, sunlight harvesting, SPR effect and charge separation efficiency, could serve as a suitable photocatalyst for biomass photoreforming.

The catalyst morphology was then investigated by SEM and TEM. The hierarchical 3DOM structure could clearly be observed by both SEM (Fig. S6) and high annular dark field (HAADF-STEM) (Fig. 3a) while the Au NPs exhibited uniform distribution in the 3DOM framework (Fig. 3a and S7). This indicates the 3DOM structure was preserved even after the introduction of Au NPs and CdS. Au NPs are in the diameter of around 15 nm and the 3DOM structure is mainly constructed by numerous TiO_2 nanocrystals (Fig. 3b). The corresponding selected area electron diffraction (SAED) pattern further confirm the crystal nature of TiO_2 and CdS (Fig. S7c). The intimate contacts of the three components (TiO_2 /Au/CdS) can be identified from both HR-TEM (Fig. 3b) and EDS elemental mappings (Fig. 3d-f). Combining with the EDS elemental maps and SAED results, the measured crystal plane with $d = 0.36 \text{ nm}$ corresponds to CdS (010) while the plane with $d = 0.35 \text{ nm}$ corresponds to TiO_2 (101). The HR-HAADF-STEM image (Fig. 3c) reveal that the Au NPs are partially covered by CdS which could enlarge the dual roles of Au NPs in this ternary photocatalyst as much as possible: electron transfer media and plasmonic photosensitizer [35]. The part of covered Au by CdS

could construct the charge transfer channel between CdS and TiO_2 while the part of exposed Au would enhance visible light absorption by SPR effect to provide more hot electrons.

3.3. Cellobiose photoreforming

To this end, the as-fabricated photocatalysts were used for cellobiose photoreforming study. The ternary Z-scheme 3DOM TiO_2 -Au-CdS indeed exhibited enhanced cellobiose conversion than 3DOM TiO_2 and 3DOM TiO_2 -Au as well as TiO_2 -Au-CdS without 3DOM structure, which indicated that the presence of both Z-scheme heterojunction with CdS and 3DOM hierarchical architecture could facilitate cellobiose photoreforming (Fig. 4a and Table S1). Although higher transient photocurrent was achieved by TiO_2 -Au-CdS without 3DOM structure, the higher cellobiose conversion of 3DOM TiO_2 -Au-CdS revealed the positive effect of 3DOM structure on mass diffusion to improve the reaction dynamics (Fig. S8a). Meanwhile, the enhanced charge separation by the formation of Z-scheme heterojunction was revealed by the reduced arc radius of ternary 3DOM TiO_2 -Au-CdS and TiO_2 -Au-CdS compared with pristine 3DOM TiO_2 and binary 3DOM TiO_2 -Au (Fig. S8b). It should be noticed that the Au/CdS content are almost equal in TiO_2 -Au-CdS (0.63 wt% of Au and 16.8 wt% of CdS) and 3DOM TiO_2 -Au-CdS (0.65 wt% of Au and 17.2 wt% of CdS). Although 3DOM TiO_2 -Au-CdS showed only $\sim 18\%$ improvement in cellobiose conversion calculated by catalyst weight, the sample TiO_2 -Au-CdS without 3DOM structure possessed larger specific surface area (Fig. S9). The $\sim 58\%$ improvement in cellobiose conversion calculated by surface area was achieved in presence of 3DOM structure (Fig. S10). Besides, the vital effect of Au NPs was also revealed by testing the cellobiose conversion over 3DOM TiO_2 -CdS, which demonstrated lower activity compared with 3DOM TiO_2 -Au-CdS (Fig. S11). Further cellobiose conversion could be achieved when reaction time was extended from 8 h (24.2%) to 16 h (37.5%), but slightly plateaued after 12 h (Fig. S12). Same trend was also observed in gas-phase products, where more H_2 , CO and CH_4 were produced by 3DOM TiO_2 -Au-CdS than others (Fig. 4b, S13 and Table S2). Interestingly, trace amount of ethane and ethylene could also be detected within the detection limit of gas chromatography (GC) (Fig. S14). The detected gases with carbon would come from the derivation of formic acid as CO, CH_4 and C_2H_4 were produced when formic acid was used as the substrate (Fig. S15). CO_2 should also be produced by the over-oxidation reaction of substrate and decomposition of formic acid as 3DOM TiO_2 -Au-CdS only showed 60.8% in carbon balance. The main products in the liquid phase include formic acid, glucose, glucaric acid, erythrose and arabinose, and their concentration exhibited near linear increase with cellobiose conversion (Fig. 4c). The corresponding selectivity of each product along with reaction time is shown in Fig. S16. Other products with very low concentration such as gluconic acid, glucuronic acid could also be detected within the detection limit of HPLC and the gas phase products could also be observed from the original GC signals (Fig. S17). The as-fabricated 3DOM TiO_2 -Au-CdS also demonstrated excellent photostability (Fig. 4d and Table S3). Although transition metal sulfides usually suffer from photo-corrosion, the presence of Z-scheme heterojunction structure and biomass derived components as the electron donor may synergistically inhibit the self-oxidation of CdS during photocatalysis. The high stability of CdS could be further revealed by the same chemical state of sulfur after reaction and XRD patterns (Figs. S18 and S19). Control experiment was also conducted by separating photocatalyst from the solution after reaction and adding AgNO_3 solution. No precipitate of Ag_2S was observed, indicating that there was no leaching S^{2-} during the photocatalytic reaction (Fig. S20). Besides, the apparent quantum yield (AQY) was calculated according to the H_2 production under 450 nm monochromatic light in presence of cellobiose and $\text{Na}_2\text{S}/\text{Na}_2\text{SO}_3$ respectively (Fig. S21). Limited AQY value was achieved in presence of cellobiose due to the complex property of cellobiose as electron donor and side reaction of photogenerated electrons such as oxygen reduction reaction to produce superoxide radicals.

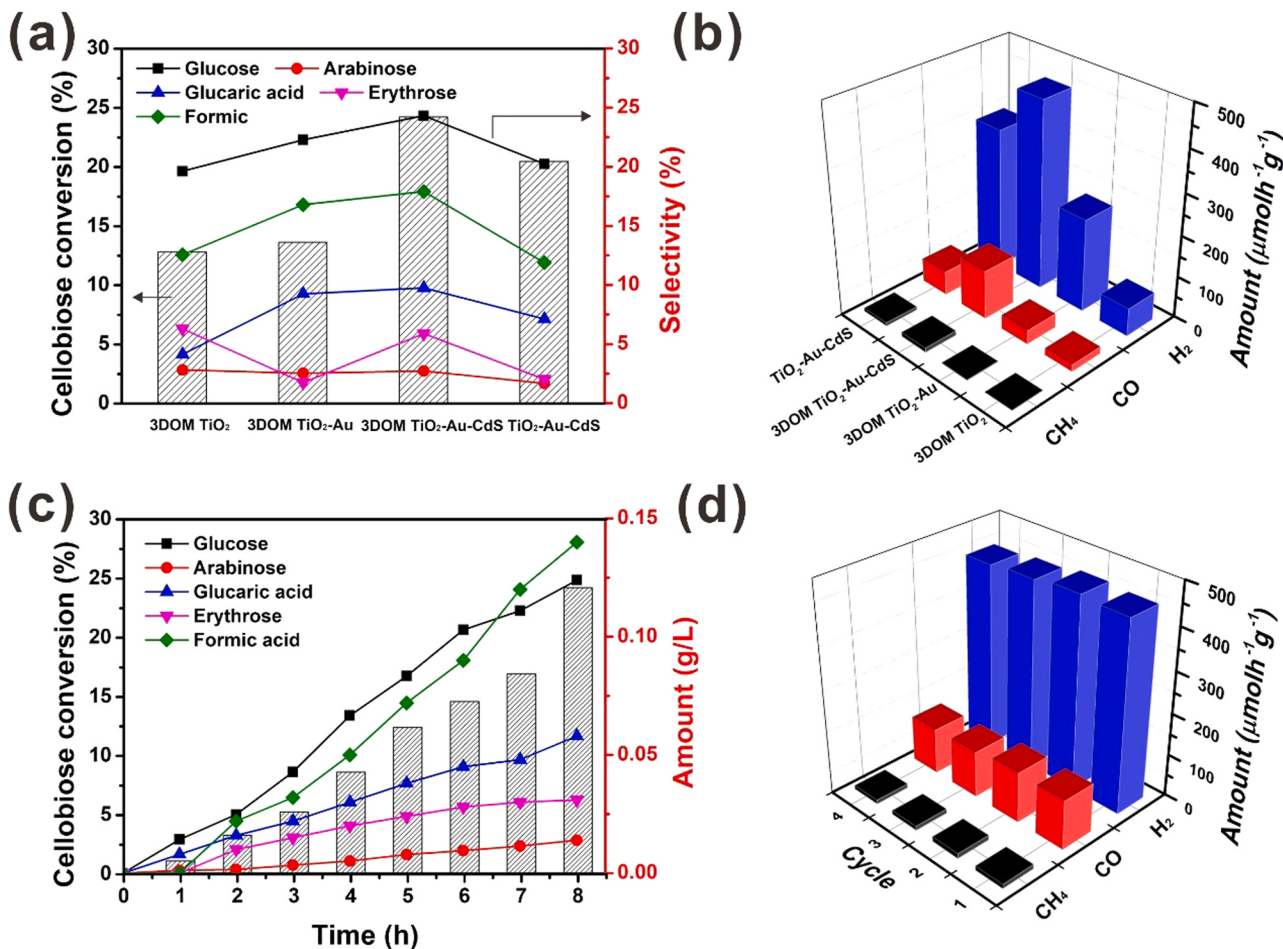


Fig. 4. (a) Cellulose conversion (after 8 h reaction) and liquid-phase products, and (b) gas-phase products distribution of different photocatalysts, (c) cellulose conversion and products distribution with reaction time for 3DOM TiO₂-Au-CdS, (d) photostability of 3DOM TiO₂-Au-CdS evaluated by gas-phase products (8 h for each cycle). Reaction condition: 25 mL 2 g/L cellulose aqueous solution, 10 mg catalyst, room temperature, pH = 7, vacuum condition, 300W Xenon lamp. The histograms correspond to cellulose conversion in (a) and (c).

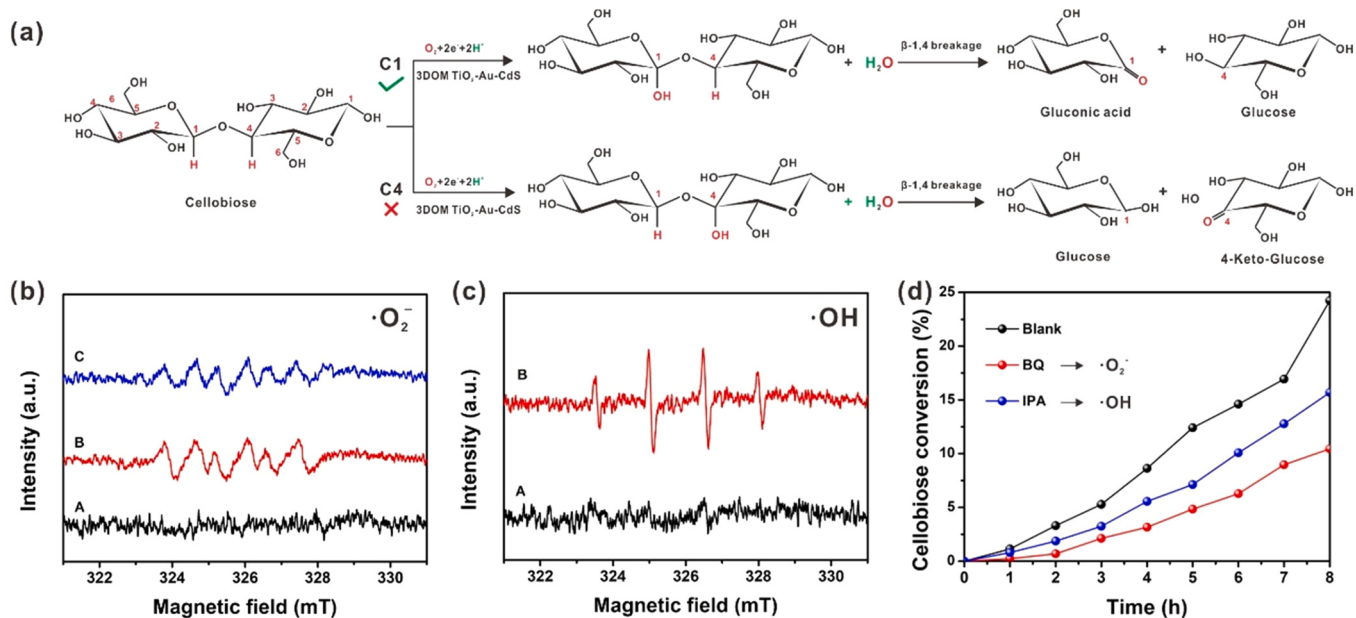


Fig. 5. Proposed reaction processes for (a) the breakage of β-1,4-glycosidic linkage, (b) ESR spin-trapping for O₂⁻ (A: under dark condition, B: under light and without oxygen purging, C: under light and with oxygen purging) and (c) ·OH (A: under dark condition, B: under light), (d) effect of different benzoquinone (BQ) and isopropanol (IPA) scavengers on cellulose conversion.

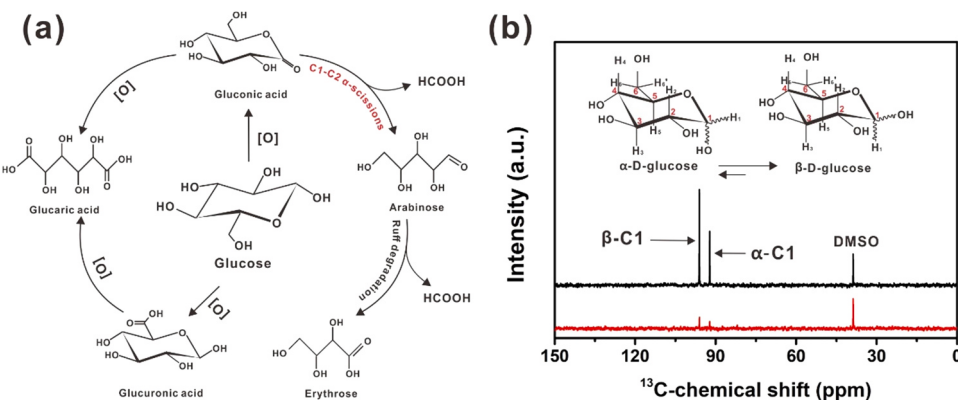


Fig. 6. (a) Proposed reaction pathway of products from cellobiose and (b) ¹³C NMR for glucose-1-¹³C before (black line) and after (red line) reaction.

The cellobiose photoreforming could be triggered by photogenerated hole and/or free radicals during photocatalysis process, where the latter one can insert oxygen at either C1 or C4 position and consequently break the β -1,4-glycosidic linkage by an elimination reaction (Fig. 5a) [45]. If the oxygen is inserted in the C1 position, the products after glycosidic bond cleavage are gluconic acid and glucose respectively, while glucose and 4-keto-glucose are produced in case of C4 position oxygen insertion. Our product distribution profile indicated the cellobiose β -1,4-glycosidic bond cleavage was initiated by free radical triggered C1 position oxygen insertion reaction pathway, since gluconic acid and glucose were produced without any 4-keto-glucose generation.

To further illustrate the reaction mechanism, the bandgap structure of 3DOM TiO₂-Au-CdS and internal charge transfer were analyzed by Mott-Schottky plots and valence band XPS to explore the potential of free radicals generation (Figs. S22a-c). It appeared that the 3DOM TiO₂-Au-CdS has enough driving force to produce both $\cdot\text{O}_2^-$ and $\cdot\text{OH}$ under UV-vis light due to the formed Z-scheme heterojunction structure (Fig. S22d) [34,36]. To confirm the generation of these radicals, the electron spin-resonance (ESR) study was performed using 5,5-dimethyl-1-pyrroline N-oxide (DMPO) as the ESR spin label for the detection of $\cdot\text{O}_2^-$ and $\cdot\text{OH}$. No signals were observed under dark condition while typical ESR signals for $\cdot\text{O}_2^-$ were generated with or without oxygen purging under irradiation (Fig. 5b). This indicates the 3DOM TiO₂-Au-CdS could produce O_2 during the reaction and the generated O_2 further reacted with photogenerated electrons to produce $\cdot\text{O}_2^-$. On the other hand, DMPO- $\cdot\text{OH}$ with typically intensity ratio of 1:2:2:1 was also observed under irradiation (Fig. 5c). Scavenger tests using benzoquinone (BQ) and isopropanol (IPA) further confirmed that both $\cdot\text{O}_2^-$ and $\cdot\text{OH}$ contributed to cellobiose photocatalytic conversion (Fig. 5d).

Glucose and gluconic acid derived from cellobiose photocatalytic conversion could then be further converted into arabinose, erythrose, formic acid and glucaric acid in the presence of radicals. Glucose could be oxidized into gluconic acid (C1 oxidation) and glucuronic acid (C6 oxidation), respectively; and both of these acids could be further oxidized into relatively stable glucaric acid (both C1 and C6 oxidized) (Fig. 6a) [46]. On the other hand, gluconic acid generated from both cellobiose oxidative cleavage and glucose oxidation could go to a different reaction pathway, where it generates arabinose via C1-C2 α -scissions and by following Ruff degradation will further yields erythrose with formic acid as side product [47]. To confirm the Ruff degradation process, ¹³C NMR was employed with dimethyl sulfoxide (DMSO) as internal standard to investigate the photoreforming of ¹³C labeled glucose at C1 position (Fig. 6b). It was clear that the intensities of α -C1 and β -C1 labeled by ¹³C significantly decreased after reaction, indicating the C1-C2 α -scissions mechanism by active oxygen species. The formed formic acid with ¹³C would be further decomposed and/or directly mineralized into CO_2 . The residual signal could correspond to the unreacted glucose with ¹³C and glucaric acid which was also derived

from ¹³C labeled glucose via oxidation reaction. To further prove the reaction pathway from glucose to gluconic acid then to arabinose, glucose and gluconic acid were used as substrates for photoreforming. One can notice that glucose was gradually consumed while gluconic acid was almost converted completely within three hours (Fig. S23). The concentration of arabinose from glucose gradually increased with reaction time while the arabinose from gluconic acid quickly reached highest concentration in three hours and then the further reaction from arabinose to erythrose by Ruff degradation reduced the arabinose concentration. This result also demonstrates that the produced gluconic acid is the intermediate product and the time-decisive step is the reaction from glucose to gluconic acid. The present work not only reveals the photocatalytic mechanism of the breakage of β -1,4-glycosidic linkage for cellobiose conversion but also provides an alternative route to produce glucaric acid which is one of the top value-added chemicals from biomass [48].

4. Conclusions

In summary, we demonstrated rational design of 3DOM TiO₂-Au-CdS Z-scheme heterojunction photocatalyst to uncover the photocatalytic mechanism for cleavage of β -1,4-glycosidic bond. Oxygen insertion at C1 position of cellobiose and then the cleavage of β -1,4-glycosidic bond to produce gluconic acid and glucose was confirmed during the photocatalytic process. The active oxygen species of cellobiose conversion were revealed to be $\cdot\text{O}_2^-$ and $\cdot\text{OH}$. These active oxygen species involved in derivation of produced glucose and/or gluconic acid into arabinose, erythrose through Ruff degradation with C1-C2 α -scissions mechanism or glucaric acid through oxidation reaction. The current work provides insights into lignocellulosic biomass valorization with solar energy utilization by facile photocatalysis.

CRediT authorship contribution statement

Heng Zhao: Investigation, Methodology, Writing – original draft, Writing – review & editing. **Chao-Fan Li:** Investigation-TEM characterization. **Xinti Yu:** Methodology, Investigation. **Na Zhong:** Methodology, Investigation. **Zhi-Yi Hu:** Investigation-TEM characterization, Writing – review & editing. **Yu Li:** Resources, Writing – review & editing. **Stephen Larter:** Writing – review & editing. **Md Golam Kibria:** Supervision, Validation, Writing editing. **Jinguang Hu:** Project administration, Supervision, Validation, Writing – review & editing, Funding acquisition.

Declaration of Competing Interest

The authors declare that they have no known competing financial interests or personal relationships that could have appeared to influence

the work reported in this paper.

Acknowledgements

We acknowledge the financial supported from the Canada First Research Excellence Fund (CFREF), Hubei Provincial Natural Science Foundation of China (2020CFB416) and the Fundamental Research Funds for the Central Universities (WUT: 2021III016GX).

Appendix A. Supporting information

Supplementary data associated with this article can be found in the online version at [doi:10.1016/j.apcatb.2021.120872](https://doi.org/10.1016/j.apcatb.2021.120872).

References

- [1] Y.H. Liao, S.F. Koelewijn, G. Van den Bossche, J. Van Aelst, S. Van den Bosch, T. Renders, K. Navare, T. Nicolai, K. Van Aelst, M. Maesen, H. Matsushima, J. M. Thevelein, K. Van Acker, B. Lagrain, D. Verboekend, B.F. Sels, A sustainable wood biorefinery for low-carbon footprint chemicals production, *Science* 367 (2020) 1385–1390.
- [2] S. Gazi, Valorization of wood biomass-lignin via selective bond scission: a minireview, *Appl. Catal. B-Environ.* 257 (2019), 117936.
- [3] T. Butburee, P. Chakthranont, C. Phawa, K. Faungnawakij, Beyond artificial photosynthesis: prospects on photobiorefinery, *ChemCatChem* 12 (2020) 1873–1890.
- [4] H. Zhao, C.F. Li, L.Y. Liu, B. Palma, Z.Y. Hu, S. Rennecker, S. Larter, Y. Li, M. G. Kibria, J.G. Hu, B.L. Su, n-p Heterojunction of TiO₂-NiO core-shell structure for efficient hydrogen generation and lignin photoreforming, *J. Colloid Interf. Sci.* 585 (2021) 694–704.
- [5] Y.B. Lu, Z.H. Zhang, H.M. Wang, Y. Wang, Toward efficient single-atom catalysts for renewable fuels and chemicals production from biomass and CO₂, *Appl. Catal. B-Environ.* 292 (2021), 120162.
- [6] J. Ma, Y. Li, D. Jin, X. Yang, G. Jiao, K. Liu, S. Sun, J. Zhou, R. Sun, Reasonable regulation of carbon/nitride ratio in carbon nitride for efficient photocatalytic reforming of biomass-derived feedstocks to lactic acid, *Appl. Catal. B-Environ.* 299 (2021), 120698.
- [7] J.L. Ma, D. Jin, X.P. Yang, S.L. Sun, J.H. Zhou, R.C. Sun, Phosphorus-doped carbon nitride with grafted sulfonic acid groups for efficient photocatalytic synthesis of xylonic acid, *Green. Chem.* 23 (2021) 4150–4160.
- [8] J.L. Ma, D. Jin, Y.C. Li, D.Q. Xiao, G.J. Jiao, Q. Liu, Y.Z. Guo, L.P. Xiao, X.H. Chen, X.Z. Li, J.H. Zhou, R.C. Sun, Photocatalytic conversion of biomass-based monosaccharides to lactic acid by ultrathin porous oxygen doped carbon nitride, *Appl. Catal. B-Environ.* 283 (2021), 119520.
- [9] S.L. Kollmannsberger, C.A. Walenta, C. Courtois, M. Tschurl, U. Heiz, Thermal control of selectivity in photocatalytic, water-free alcohol photoreforming, *ACS Catal.* 8 (2018) 11076–11084.
- [10] M. Zhang, Z. Li, X. Xin, J.H. Zhang, Y.Q. Feng, H.J. Lv, Selective valorization of 5-hydroxymethylfurfural to 2,5-diformylfuran using atmospheric O₂ and MAPbBr₃ Perovskite under visible light, *ACS Catal.* 10 (2020) 14793–14800.
- [11] M.F. Kuehnel, E. Reisner, Solar hydrogen generation from lignocellulose, *Angew. Chem. Int. Ed.* 57 (2018) 3290–3296.
- [12] H. Kasap, D.S. Achilleos, A. Huang, E. Reisner, Photoreforming of lignocellulose into H₂ using nanoengineered carbon nitride under benign conditions, *J. Am. Chem. Soc.* 140 (2018) 11604–11607.
- [13] D.W. Wakerley, M.F. Kuehnel, K.L. Orchard, K.H. Ly, T.E. Rosser, E. Reisner, Solar-driven reforming of lignocellulose to H₂ with a CdS/CdOx photocatalyst, *Nat. Energy* 2 (2017) 1–9.
- [14] X.X. Wu, H. Zhao, M.A. Khan, P. Maity, T. Al-Attas, S. Larter, Q. Yong, O. F. Mohammed, M.G. Kibria, J.G. Hu, Sunlight-driven biomass photorefinery for coproduction of sustainable hydrogen and value-added biochemicals, *ACS Sustain. Chem. Eng.* 8 (2020) 15772–15781.
- [15] U. Nwosu, A. Wang, B. Palma, H. Zhao, M.A. Khan, M. Kibria, J. Hu, Selective biomass photoreforming for valuable chemicals and fuels: a critical review, *Renew. Sust. Energ. Rev.* 148 (2021), 111266.
- [16] Y.T. Liu, G.Y. Li, Y.C. Hu, A.Q. Wang, F. Lu, J.J. Zou, Y. Cong, N. Li, T. Zhang, Improved druggability of gambogic acid using core-shell nanoparticles, *Joule* 3 (2019) 1028–1036.
- [17] D. Klemm, B. Heublein, H.P. Fink, A. Bohn, Cellulose: fascinating biopolymer and sustainable raw material, *Angew. Chem. Int. Ed.* 44 (2005) 3358–3393.
- [18] L. Da Via, C. Recchi, T.E. Davies, N. Greeves, J.A. Lopez-Sanchez, Visible-light-controlled oxidation of glucose using titania-supported silver photocatalysts, *ChemCatChem* 8 (2016) 3475–3483.
- [19] R.F. Chong, J. Li, Y. Ma, B. Zhang, H.X. Han, C. Li, Selective conversion of aqueous glucose to value-added sugar aldehyde on TiO₂-based photocatalysts, *J. Catal.* 314 (2014) 101–108.
- [20] J.L. Ma, Y.C. Li, D. Jin, Z. Ali, G.J. Jiao, J.Q. Zhang, S. Wang, R.C. Sun, Functional B@mCN-assisted photocatalytic oxidation of biomass-derived pentoses and hexoses to lactic acid, *Green. Chem.* 22 (2020) 6384–6392.
- [21] C.F. Shao, Q. Shao, X.Y. Wang, J. Ling, X. Guo, Y.L. Ning, Y.J. Dai, S.R. Jia, Y. Qiao, C.W. Li, K. Zhao, Study on cellulose degradation induced by hydroxyl radical with cellobiose as a model using GC-MS, ReaxFF simulation and DFT computation, *Carbohyd. Polym.* 233 (2020), 115677.
- [22] A.P.S. Brogan, L. Bui-Le, J.P. Hallett, Non-aqueous homogenous biocatalytic conversion of polysaccharides in ionic liquids using chemically modified glucosidase, *Nat. Chem.* 10 (2018) 859–865.
- [23] W. Yin, Z.C. Tang, R.H. Venderbosch, Z. Zhang, C. Cannilla, G. Bonura, F. Frusteri, H.J. Heeres, A one-step synthesis of C6 sugar alcohols from levoglucosan and disaccharides using a Ru/CMK-3 catalyst, *ACS Catal.* 6 (2016) 4411–4422.
- [24] B. Zhang, J. Li, L. Guo, Z.P. Chen, C. Li, Photothermally promoted cleavage of β -1,4-glycosidic bonds of cellulosic biomass on Ir/HY catalyst under mild conditions, *Appl. Catal. B-Environ.* 237 (2018) 660–664.
- [25] Y. Yang, H. Qi, H. Li, Z. Xu, X. Liu, S. Yu, Z.C. Zhang, Heterometallic PdII-Cl-CuI catalyst for efficient hydrolysis of β -1,4-glycosidic bonds in 1-butyl-3-methylimidazolium chloride, *ACS Catal.* 11 (2021) 11774–11785.
- [26] X.J. Wu, J.Q. Li, S.J. Xie, P.B. Duan, H.K. Zhang, J. Feng, Q.H. Zhang, J. Cheng, Y. Wang, Selectivity control in photocatalytic valorization of biomass-derived platform compounds by surface engineering of titanium oxide, *Chem* 6 (2020) 3038–3053.
- [27] M. Melchionna, P. Fornasiero, Updates on the roadmap for photocatalysis, *ACS Catal.* 10 (2020) 5493–5501.
- [28] J. Liu, H. Zhao, M. Wu, B. Van der Schueren, Y. Li, O. Deparis, J.H. Ye, G.A. Ozin, T. Hasan, B.L. Su, Slow photons for photocatalysis and photovoltaics, *Adv. Mater.* 29 (2017), 1605349.
- [29] H. Zhao, Z.Y. Hu, J. Liu, Y. Li, M. Wu, G. Van Tendeloo, B.L. Su, Blue-edge slow photons promoting visible-light hydrogen production on gradient ternary 3DOM TiO₂-Au-CdS photonic crystals, *Nano Energy* 47 (2018) 266–274.
- [30] X.F. Zheng, G.F. Shen, C. Wang, Y. Li, D. Dunphy, T. Hasan, C.J. Brinker, B.L. Su, In situ click chemistry generation of cyclooxygenase-2 inhibitors, *Nat. Commun.* 8 (2017) 1–9.
- [31] L.H. Chen, Y. Li, B.L. Su, Hierarchy in materials for maximized efficiency, *Natl. Sci. Rev.* 7 (2020) 1626–1630.
- [32] S.J.A. Moniz, S.A. Shevlin, D.J. Martin, Z.X. Guo, J.W. Tang, Visible-light driven heterojunction photocatalysts for water splitting – a critical review, *Energ. Environ. Sci.* 8 (2015) 731–759.
- [33] D.L. Huang, Z.H. Li, G.M. Zeng, C.Y. Zhou, W.J. Xue, X.M. Gong, X.L. Yan, S. Chen, W.J. Wang, M. Cheng, Megamerger in photocatalytic field: 2D g-C₃N₄ nanosheets serve as support of 0D nanomaterials for improving photocatalytic performance, *Appl. Catal. B-Environ.* 240 (2019) 153–173.
- [34] H. Tada, T. Mitsui, T. Kiyonaga, T. Akita, K. Tanaka, All-solid-state Z-scheme in CdS-Au-TiO₂ three-component nanojunction system, *Nat. Mater.* 5 (2006) 782–786.
- [35] J.T. Li, S.K. Cushing, P. Zheng, T. Senty, F.K. Meng, A.D. Bristow, A. Manivannan, N.Q. Wu, Solar hydrogen generation by a CdS-Au-TiO₂ sandwich nanorod array enhanced with Au nanoparticle as electron relay and plasmonic photosensitizer, *J. Am. Chem. Soc.* 136 (2014) 8438–8449.
- [36] H. Zhao, M. Wu, J. Liu, Z. Deng, Y. Li, B.L. Su, Synergistic promotion of solar-driven H₂ generation by three-dimensionally ordered macroporous structured TiO₂-Au-CdS ternary photocatalyst, *Appl. Catal. B-Environ.* 184 (2016) 182–190.
- [37] M. Jourshabani, B.K. Lee, Z. Sharatinia, From traditional strategies to Z-scheme configuration in graphitic carbon nitride photocatalysts: recent progress and future challenges, *Appl. Catal. B-Environ.* 276 (2020), 119157.
- [38] X. Ma, G.W. Wang, L.F. Qin, J. Liu, B. Li, Y.A. Hu, H.F. Cheng, Z-scheme g-C₃N₄-AQ-MoO₃ photocatalyst with unique electron transfer channel and large reduction area for enhanced sunlight photocatalytic hydrogen production, *Appl. Catal. B-Environ.* 288 (2021), 120025.
- [39] B. Wang, J.Z. Zhao, H.L. Chen, Y.X. Weng, H. Tang, Z.R. Chen, W.S. Zhu, Y.B. She, J.X. Xia, H.M. Li, Unique Z-scheme carbonized polymer dots/Bi₂O₃Br₂ hybrids for efficiently boosting photocatalytic CO₂ reduction, *Appl. Catal. B-Environ.* 293 (2021), 120182.
- [40] Y.F. Zhou, M.C. Yu, H.J. Liang, J. Chen, L. Xu, J.F. Niu, Novel dual-effective Z-scheme heterojunction with g-C₃N₄, Ti₃C₂ MXene and black phosphorus for improving visible light-induced degradation of ciprofloxacin, *Appl. Catal. B-Environ.* 291 (2021), 120105.
- [41] H. Zhao, C.-F. Li, Z.-Y. Hu, J. Liu, Y. Li, J. Hu, G. Van Tendeloo, L.-H. Chen, B.-L. Su, Size effect of bifunctional gold in hierarchical titanium oxide-gold-cadmium sulfide with slow photon effect for unprecedented visible-light hydrogen production, *J. Colloid Interf. Sci.* 604 (2021) 131–140.
- [42] H. Zhao, P. Liu, X. Wu, A. Wang, D. Zheng, S. Wang, Z. Chen, S. Larter, Y. Li, B.-L. Su, M.G. Kibria, J. Hu, Plasmon enhanced glucose photoreforming for arabinose and gas fuel co-production over 3DOM TiO₂-Au, *Appl. Catal. B-Environ.* 291 (2021), 120055.
- [43] X.Q. Liu, J. Icozzetta, Y. Wang, X. Cui, Y.H. Chen, S.Q. Zhao, Z. Li, Z.Q. Lin, Noble metal–metal oxide nanohybrids with tailored nanostructures for efficient solar energy conversion, photocatalysis and environmental remediation, *Energ. Environ. Sci.* 10 (2017) 402–434.
- [44] T. Ming, L. Zhao, Z. Yang, H.J. Chen, L.D. Sun, J.F. Wang, C.H. Yan, Strong polarization dependence of plasmon-enhanced fluorescence on single gold nanorods, *Nano Lett.* 9 (2009) 3896–3903.
- [45] W.T. Beeson, C.M. Phillips, J.H.D. Cate, M.A. Marletta, Oxidative cleavage of cellulose by fungal copper-dependent polysaccharide monooxygenases, *J. Am. Chem. Soc.* 134 (2012) 890–892.

[46] R. Wojcieszak, I.M. Cuccovia, M.A. Silva, L.M. Rossi, Selective oxidation of glucose to glucuronic acid by cesium-promoted gold nanoparticle catalyst, *J. Mol. Catal. A-Chem.* 422 (2016) 35–42.

[47] J.A. Stapley, J.N. BeMiller, The Ruff degradation: a review of previously proposed mechanisms with evidence that the reaction proceeds by a Hofer-Moest-type reaction, *Carbohydr. Res.* 342 (2007) 407–418.

[48] A.J. Ragauskas, C.K. Williams, B.H. Davison, G. Britovsek, J. Cairney, C.A. Eckert, W.J. Frederick, J.P. Hallett, D.J. Leak, C.L. Liotta, J.R. Mielenz, R. Murphy, R. Templer, T. Tschaplinski, The path forward for biofuels and biomaterials, *Science* 311 (2006) 484–489.